nature communications

Article

https://doi.org/10.1038/s41467-026-69257-8

Cooperative anion activation at a cobalt center through ion pairing and ligand design

Received: 24 July 2025

Accepted: 26 January 2026

Published online: 07 February 2026

Check for updates

Luis Tarifa[1,2], Judit Cano-Asensio[1,2], José A. López[1], Cristina Tejel[1] & Ana M. Geer[1]

Weakly coordinating anions (WCAs) are commonly used to stabilize high-valent, electrophilic transition-metal complexes, owing to their low nucleophilicity and minimal coordinating ability. Here, we present a cobalt platform supported by a tris(2-pyridyl)(N-picolyl)imidazolidine ligand (Py_4Im) that generates a directional, protic cavity for ion pairing. This environment enables a comparative study of BF_4^- and PF_6^-, showing that PF_6^- undergoes fluoride abstraction under mild conditions, while BF_4^- remains unreactive unless assisted by a Lewis base. The PF_6^- activation yields a well-defined Co^{III}–F complex that acts as an efficient nucleophilic fluoride source. DFT calculations and diffusion NMR experiments highlight the critical role of anion-cation pairing in modulating reactivity, overriding intrinsic thermodynamic preferences. These findings showcase supramolecular control of WCA activation by a late transition metal and provide new design principles for reactivity modulation via counterion selection.

Electrophilic activation of substrates by transition-metal catalysts is a fundamental step in the activation of small molecules and homogeneous catalysis[1–4]. Enhancing the electrophilic nature (or Lewis acidity) of the metal center, particularly in cationic complexes of late transition metals, has enabled the transformation of otherwise inert substrates through nucleophilic attack. This electrophilic reactivity underpins key processes such as hydrogenation, C–H bond functionalization, olefin oligomerization, and industrially relevant reactions like the Wacker process[5,6].

Given their reactivity, there is considerable interest in developing high-valent (>+2), cationic transition-metal complexes with strong electrophilic character. However, these species often suffer from low stability and poor solubility in organic solvents. The use of multidentate macrocyclic ligands, which stabilize the metal center and enhance solubility, is a common strategy to address these challenges.

Despite this, structurally defined Co^{III} complexes with high electrophilicity and without cyclopentadienyl (Cp*) ligands remain rare[7,8]. A relevant example by Ribas and coworkers invoked a macrocyclic-stabilized Co^{III} electrophilic intermediate in C–H annulation chemistry[9]. Recently, tetra-amido macrocyclic ligands have also been employed to stabilize Co^{III} centers involved in single-electron redox processes[10,11]. Related oxidative Co^{III} reactivity has been demonstrated in aminoquinoline-directed C–H functionalization using simple Co^{II} precursors[12]. Complementing these advances, Das and co-workers have shown that cobalt complexes supported by polydentate N-donor ligands can reach even higher oxidation levels, including $Co^{IV}(F)_2$ and Co^{III}–F species capable of C–H activation and fluorine-atom transfer[13].

In designing such complexes, the choice of counterion is critical. Anions such as MF_6^- (M = P, As, Sb) and BF_4^- are widely used due to their perceived non-coordinating nature[14]. These anions were later found to possess some coordination ability, leading to their classification as weakly coordinating anions (WCAs)[15].

WCAs are crucial in stabilizing highly charged, oxidizing cations. Ideal WCAs exhibit minimal interaction with the cation, remaining non-coordinating, non-nucleophilic, and highly resistant to oxidation; three properties that are intrinsically interlinked[15]. Their weak cation-anion interactions reduce ion pairing in solution, a property also valuable in battery electrolytes (including lithium-ion batteries)[16] and in ionic liquids[17].

However, their weak coordinating ability has limited structural characterization[14]. To date, only four structurally characterized mononuclear Co^{II}-BF_4^- and two Co^{II}-PF_6^- are reported in the

[1]Instituto de Síntesis Química y Catálisis Homogénea (ISQCH), Departamento de Química Inorgánica, CSIC-Universidad de Zaragoza, Pedro Cerbuna 12, 50009 Zaragoza, Spain. [2]These authors contributed equally: Luis Tarifa, Judit Cano-Asensio. e-mail: ctejel@unizar.es; anageer@unizar.es

Cambridge Structural Database (CSD)[18–20], and none for Co(III) with either anion (Fig. 1A)[21].

Fluoride abstraction from WCAs, especially BF_4^-, has gained attention as a means to access metal–fluoride complexes or to enable catalytic transformations[18,22,23]. BF_4^- is generally more prone to fluoride abstraction than PF_6^-, consistent with the lower fluoride ion affinity (FIA) value of BF_3 compared to PF_5[24]. While BF_4^- activation has been used synthetically and catalytically[18,23,25,26], PF_6^- activation is rare and usually requires high temperatures or highly Lewis acidic environments[27–31]. For cobalt, only one report describes PF_6^- activation, where the fluoride abstraction is mediated by a more Lewis acidic Zr-oxo unit, with Co playing a spectator role[32].

Beyond their role as spectator anions, WCAs may also act as fluoride sources in C–F bond formation[33–35]. While BF_4^- has shown promise in this regard, sometimes acting as a fluoride shuttle, the use of PF_6^- in such contexts remains underexplored[22,26,28].

The different reactivities of BF_4^- and PF_6^- illustrate the importance of selecting an appropriate WCA to modulate the stability and reactivity of electrophilic cationic species. Understanding these subtle distinctions is essential not only for designing robust catalysts but also for elucidating fundamental aspects of anion coordination and reactivity.

Herein, we report a tris(2-pyridyl)(N-picolyl)imidazolidine ligand (Py_4Im) platform that stabilizes Co^{II} and Co^{III} species in highly electrophilic environments. The Py_4Im ligand, formed in situ through dimerization of bpi, features a protic imidazolidine cavity and rigid macrocyclic geometry that creates a directional binding pocket for counteranions. We show that while PF_6^- undergoes fluoride abstraction under mild conditions to give a Co–F complex, BF_4^- remains unreactive unless assisted by a Lewis base. Structural, spectroscopic, and computational analyses provide rare mechanistic insight into WCA activation by a late transition metal. This work sheds light on the role of ion pairing and coordination dynamics in modulating reactivity and suggests new strategies for leveraging WCAs as fluoride sources in catalysis.

Results

Synthesis and characterization of Co^{II} species

Initial experiments were conducted by reacting the imine Py-CH_2N = CHPy (Py = 2-pyridyl, bpi) with the cobalt precursor $CoCl_2$ in CH_3CN, initially yielding the expected product $[Co(\kappa^3\text{-bpi})Cl_2]$ (**1**) in 48% yield as a forest green solid (Fig. 1B). The magnetic moment of complex **1** determined by Evans' NMR (μ_{eff} = 3.88) is consistent with a Co^{II} center in a high-spin (S = 3/2) configuration. The wide-scan ^{1}H NMR spectra of **1** in dmso-d_6 display 11 paramagnetically shifted resonances from 154 to −0.8 ppm corresponding to a coordinated bpi ligand to the cobalt center (Fig. S1). Interestingly, during monitoring of complex **1** stability in dmso-d_6 solution by ^{1}H NMR spectroscopy, we observed its clean conversion into a distinct paramagnetic species after 24 h at 25 °C (Fig. S21). The newly formed species exhibits 22 inequivalent proton resonances ranging from 207 to −37 ppm (Fig. S2). A preparative-scale reaction in methanol using a 2:1.5 molar ratio of bpi to $CoCl_2$ successfully produced the novel species as a blue solid in excellent yield (91%).

Single-crystal X-ray diffraction analysis of blue crystals isolated from the reaction mixture identified this species as $[Co(\kappa^5\text{-}Py_4Im)Cl]_2[CoCl_4]$ ($[\mathbf{2}]_2[CoCl_4]$; Py_4Im = 2,2′,2″-(1-(pyridin-2-ylmethyl)imidazolidine-2,4,5-triyl)tripyridine), Fig. 1C. Notably, complex **2** now contains a tetra-substituted imidazolidine-based macrocyclic ligand, Py_4Im, formed by dimerization of bpi through a 1,3-dipolar cycloaddition[36,37]. Py_4Im acts as a macrocyclic ligand containing nitrogen-donor atoms, similar to those previously reported to stabilize transition metal complexes in high oxidation states[38].

The solid-state structure features the cobalt in an octahedral coordination environment, bonded to four pyridine nitrogen atoms on an equatorial plane, with the axial positions occupied by the bridging

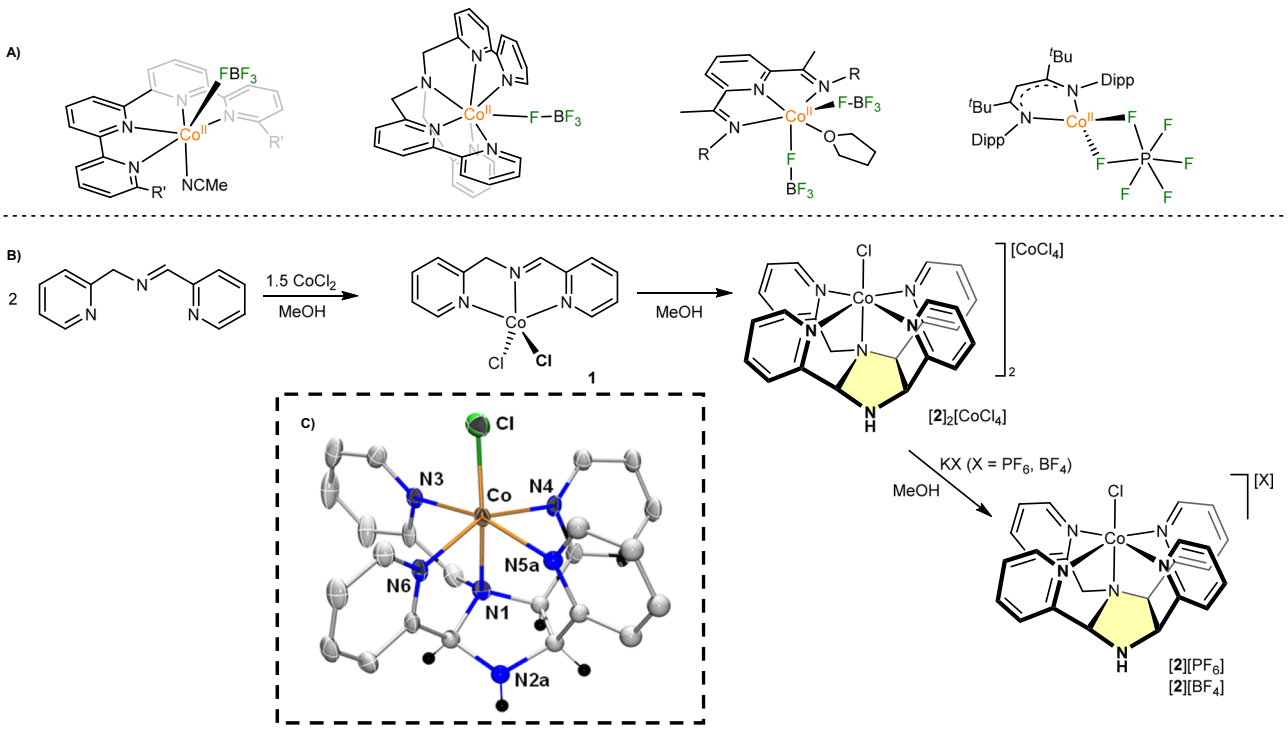

Fig. 1 | Overview of cobalt-mediated anion interactions and cobalt platform synthesis. A Selected examples of BF_4^- and PF_6^- coordination to cobalt found in the CSD database (accessed on 20/06/2025). **B** Synthesis of complexes $[Co(\kappa^3\text{-bpi})Cl_2]$ (**1**), $[Co(\kappa^5\text{-}Py_4Im)Cl]_2[CoCl_4]$ ($[\mathbf{2}]_2[CoCl_4]$) and [**2**][X] (X = PF_6^-, BF_4^-). **C** Crystal structure of $[Co(\kappa^5\text{-}Py_4Im)Cl]_2[CoCl_4]$ ($[\mathbf{2}]_2[CoCl_4]$) with displacement ellipsoids set to 50%. Only hydrogen atoms on the imidazolidine ring are shown. Minor disorder components and the anion are omitted for clarity.

https://doi.org/10.1038/s41467-026-69257-8

A)

Signal	δ (ppm)	$LW_{1/2}$ (Hz)	T_1 exp. (ms)
1	206.6	194	1.9
2	199.5	106	4.0
3	181.7	185	1.8
4	170.3	150	3.3
5	166.1	110	4.4
6	122.8	277	0.9
7	78.9	140	2.4
8	72.7	25	19.0
9	70.4	18	40.1
10	68.4	18	40.1
11	59.5	20	24.1
12	54.8	22	21.1
13	24.5	19	26.7
14	22.5	14	82.6
15	21.8	14	72.2
16	20.9	17	26.0
17	19.1	19	22.8
18	1.7	194[a]	-[b]
19	-0.6	15	62.6
20	-5.7	15	71.0
21	-26.3	145	3.1
22	-31.9	78	6.6

[a] The linewidth at half-height ($LW_{½}$) was measured at 0 °C because peak overlap occurred at 25 °C. [b] T_1 could not be determined due to peak overlap of signal 18 at 25 °C.

B)

Proton[a]	Type of proton	$r_{Co,H}$ (Å)[b]	$r_{Co,H}^{-6}$	T_1 estim. (ms)[c]	T_1 exp. (ms)	Signals
H19	(Py-H^6)	3.122	9.25E+02	1.7	0.9	**Py-H^6**
H24	(Py-H^6)	3.186	1.05E+03	2.0	1.8	
H9	(Py-H^6)	3.195	1.06E+03	2.0	1.9	6, 3, 1, 18
H14	(Py-H^6)	3.240	1.16E+03	2.2	-	
H4b	CH_2	3.360	1.45E+03	2.7	2.4	
H1	CH	3.829	3.15E+03	5.9	3.1	**Im**
H3	CH	3.846	3.23E+03	6.1	3.3	
H4a	CH_2	3.839	3.20E+03	6.0	4.0	7, 4, 2, 5, 22
H2	CH	4.325	6.54E+03	12.3	4.4	
NH	NH	4.492	8.21E+03	15.4[d]	6.6	21 (**NH**)
H11	(Py-$H^{3/5}$)	4.949	1.47E+04	27.7	19.0	
H21	(Py-$H^{3/5}$)	4.990	1.54E+04	29.0	21.1	**Py-$H^{3/5}$**
H6	(Py-$H^{3/5}$)	4.992	1.55E+04	29.2	22.8	
H8	(Py-$H^{3/5}$)	5.146	1.86E+04	35.0	24.1	12, 11, 8,
H18	(Py-$H^{3/5}$)	5.154	1.87E+04	35.2	26.0	10, 13, 9,
H23	(Py-$H^{3/5}$)	5.162	1.89E+04	35.6	26.7	17, 16
H13	(Py-$H^{3/5}$)	5.177	1.93E+04	36.3	40.1	
H16	(Py-$H^{3/5}$)	5.211	2.00E+04	37.6	40.1	
H12	(Py-H^4)	5.815	3.87E+04	72.8	62.6	**Py-H^4**
H7	(Py-H^4)	5.835	3.94E+04	74.1	71.0	
H22	(Py-H^4)	5.842	3.97E+04	74.7	72.2	14, 15,
H17	(Py-H^4)	5.939	**4.39E+04**	**82.6**	**82.6**	20, 19

[a] Labels for hydrogen atoms are shown in Figure S27. [b] Distance between hydrogen and cobalt calculated from the crystallographic data. [c] The estimated T_1 values were obtained by normalizing $[\Sigma(r_{Co,H})^{-6}]^{-1}$ to the experimental T_1 value of the signal with the largest value (signal 14, proton H17). [d] The large discrepancy between the experimental and estimated T_1 values for the NH can be attributed to the contribution of the quadrupolar moment of the nitrogen atom, an effect not applicable to the other protons.

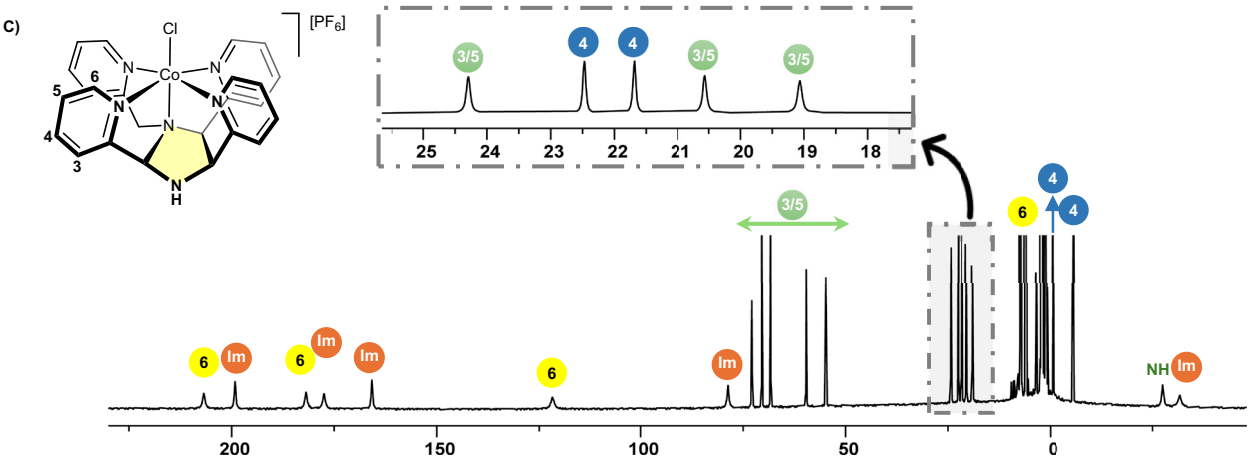

Fig. 2 | Paramagnetic ^{1}H NMR analysis and signal assignment of [2][PF_6]. **A** Chemical shifts of [2][PF_6] from ^{1}H NMR data, linewidths at half-height (LW½), and measured T_1 relaxation times. **B** Distances between the hydrogen atoms and the cobalt center derived from crystallographic data, estimated T_1 relaxation times, and the corresponding assignments by proton type. **C** ^{1}H NMR (300 MHz, CD_3CN, 25 °C) spectrum of [2][PF_6] with assignments based on T_1 relaxation measurements.

nitrogen of the imidazolidine ring and a chloride atom. Three of the Co-N_{Py} (N3, N4 and N6) bond distances are *ca.* 2.14 Å, consistent with other Co^{II} high-spin species[39–41]. The crystallographic analysis also provided insight into the stereochemistry of the imidazolidine ring formed in the reaction, which adopts an all-*cis* substitution pattern, specifically the 4,5-*endo*,2,4-*cis* isomer (Fig. 1C). This result contrasts previous reports of bpi dimerization, which predominantly yield the 4,5-*exo* isomer[42–45]. In our system, the cobalt center likely templates the ring closure, favoring the all-*cis* configuration.

In the next step, the $CoCl_4^{2-}$ counterion was exchanged for a WCA (PF_6^- or BF_4^-) through a salt metathesis reaction by adding an excess KPF_6 or $NaBF_4$, respectively, yielding the corresponding [2][PF_6] and [2][BF_4] salts, respectively. The ^{1}H NMR spectra of [2][X] (X = PF_6^-, BF_4^-) are very similar to that of [2]$_2$[$CoCl_4$] (Fig. S2). For [2][PF_6], the paramagnetic ^{1}H NMR spectrum was analyzed and assigned using a combination of methods: T_1 relaxation time measurements, D_2O shake experiments, and two-dimensional ^{1}H-^{1}H homonuclear correlation spectroscopy (COSY) NMR spectroscopy.

T_1 relaxation times were correlated with metal-proton distances from crystallographic data using the simplified version of Solomon-Bloembergen equation[46], which relates relaxation rate (T_1^{-1}) to the inverse sixth power of the metal-proton distance ($r_{Co,H}^{-6}$)[47–50]. The ^{1}H NMR spectra of [2][PF_6] reveal a wide range of signal broadness with linewidths at half-height ($LW_{½}$) varying from 14 to 277 Hz (Fig. 2A) and corresponding T_1 values from 0.9 to 82.6 ms (Fig. 2A), reflecting varying proximities to the paramagnetic center. To aid signal assignment, protons were grouped by T_1 values, enabling classification based on their proximity to the metal center (Fig. 2B). Protons with measured $T_1 < 1.9$ ms are attributed to H^6-Py protons on the pyridine rings, which are closest to the cobalt center. Signals with experimental T_1 values between 2.4 and 6.6 ms correspond to the protons on the imidazolidine ring, while those with $T_1 > 62$ ms are assigned to the H^4-Py protons, which have the largest distances from the cobalt. Due to the similar Co···H distances of the H^3-Py and H^5-Py protons, all within the range of 4.950–5.211 Å (Fig. 2B), their signals could not be resolved.

https://doi.org/10.1038/s41467-026-69257-8

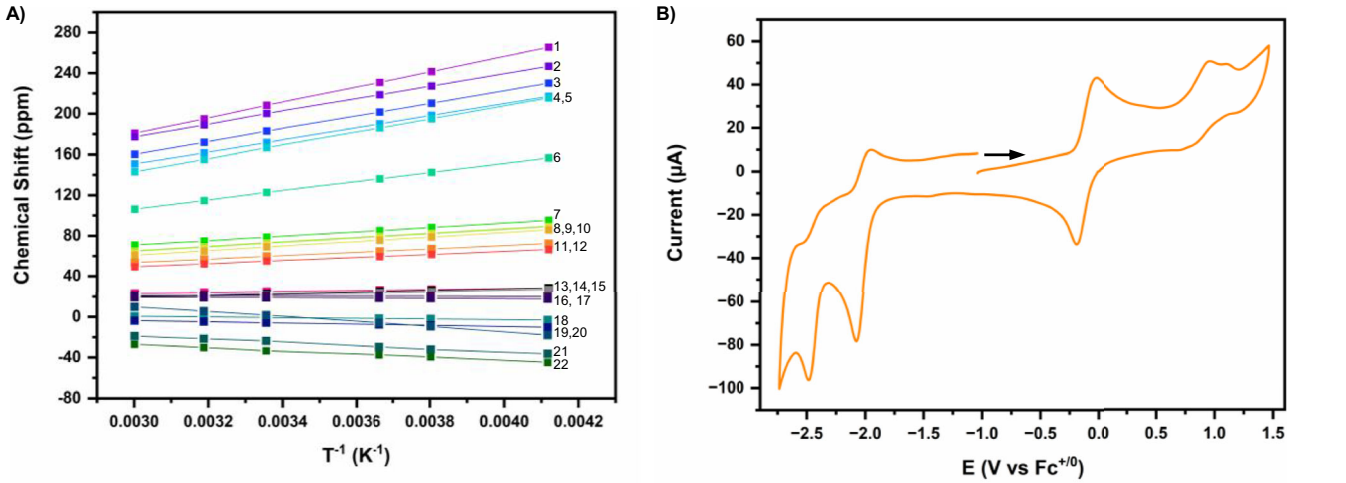

Fig. 3 | Magnetic behavior and electrochemical properties of [2][PF$_6$]. A ^{1}H NMR chemical shifts for [**2**][PF$_6$] in CD_3CN plotted versus 1/T. Numbers next to each line indicate individual proton resonances as assigned in Fig. 2; solid lines represent the connecting lines between data points (symbols). **B** Cyclic voltammogram of 1.0 mM [**2**][PF$_6$] in CH_3CN with 0.1 M [NBu_4][PF$_6$] as a supporting electrolyte recorded at 0.1 V/s scan rate.

While this grouping allows approximate classification by proton type, discrepancies arise for signals on the imidazolidine ring and CH_2. These may reflect differences between solid-state and solution distances or spin–spin dipolar interactions influencing rotational barriers (e.g., due to hydrogen bonding or ion pairing). In particular, the signals at −31.9, −26.3, and 170.3 ppm (Fig. S2), assigned to imidazolidine ring protons, are most affected, in both chemical shift and linewidths, by changes in solvent and counterion. This behavior is consistent with that observed for the Co^{III} complexes (see discussion below) and suggests involvement in anion–cation interactions.

Further NMR experiments supported these assignments. A D_2O shake confirmed the NH proton −26.3 ppm (Fig. S22), and COSY NMR enabled the identification of the H^3, H^4, and H^5-Py, confirming their placement on individual pyridine rings (Fig. S3).

The magnetic moment of [**2**][PF$_6$], determined by Evans' NMR (μ_{eff} = 4.80), is consistent with the high-spin nature of the Co^{II} center. Moreover, the chemical shifts of all proton peaks exhibit temperature dependence, with a linear relationship between chemical shift and 1/T observed from 60 °C to −30 °C. Among these, 20 peaks display Curie-Weiss behavior, typical of compounds in a pure spin state, while two peaks show anti-Curie behavior (Figs. 3A, S34).

To gain insight into the redox chemistry of [**2**][PF$_6$], the complex was investigated using cyclic voltammetry (CV). CVs of [**2**][PF$_6$] under argon in CH_3CN display a reversible one-electron oxidation feature at $E_{1/2}$ = 0.01 V (all potentials are reported vs. Fc$^{+/0}$), assigned to the metal-centered Co^{II} to Co^{III} oxidation, followed by two irreversible oxidation features with an anodic peak potential ($E_{p,a}$) of 0.95 V and 1.16 V. (Fig. 3B). At more negative potentials, two irreversible reduction features with cathodic peak potentials ($E_{p,c}$) of −2.07 V and −2.39 V are assigned to ligand-centered reductions. An analogous CV was observed for [**2**][BF$_4$] (Fig. S35).

Synthesis and characterization of Co^{III} species

The electrochemical profiles of [**2**][PF$_6$] and [**2**][BF$_4$] motivated us to explore their one-electron oxidation using chemical methods. This was achieved by the addition of a stoichiometric amount of thianthrenium hexafluorophosphate ([Th•$^+$]PF$_6$; $E_{1/2}$ = 0.86 V)[51] to [**2**][PF$_6$] and [**2**][BF$_4$] in CH_3CN. This transformation produced an immediate color change from violet to red or brown, respectively, resulting in the clean formation of [Co^{III}(κ^5-Py$_4$Im)Cl][X]$_2$ ([**3**][X]$_2$; X = PF$_6^-$, BF$_4^-$) in high yields, Fig. 4A.

The ^{1}H NMR spectra of [**3**][X]$_2$ (X = PF$_6^-$, BF$_4^-$) show the expected diamagnetic proton chemical shifts for a low-spin Co^{III} center in a d^6 configuration (Figs. S4, S7). For both complexes, the four inequivalent pyridine groups are observed in the aromatic region (9.70–7.00 ppm) and were unambiguously identified by the use of 1D-selective total correlation spectroscopy (TOCSY) NMR experiments (Fig. S5). As seen for the Co^{II} analogs, the identity of the counterion significantly influences the chemical shifts of the imidazolidine ring and CH_2 protons in the ^{1}H NMR spectra. For X = PF$_6^-$, signals appear between 5.68 and 4.36 ppm, while for X = BF$_4^-$, they appear shielded to the 4.93–3.10 ppm range. This pronounced shielding effect is attributed to stronger anion–cation interactions in the BF$_4^-$, likely involving electrostatic or hydrogen bonding effects that reduce proton electron density and result in shielding of the ^{1}H NMR signals. The N–H proton exhibits the largest shift, from 4.36 ppm (PF$_6^-$) to 3.10 ppm (BF$_4^-$), suggesting its direct participation in hydrogen bonding with the anions.

To investigate the extent of these cation–anion interactions, we studied the complexes [**3**][X]$_2$ (X = PF$_6^-$, BF$_4^-$) by ^{1}H and ^{19}F diffusion-ordered spectroscopy (DOSY) NMR. The diffusion coefficients for the cation (D^+) and anion (D^-) were estimated, and hydrodynamic radii (r_H^+ and r_H^-) were calculated using the modified Stokes–Einstein equation (Entries 2 and 3, Fig. 4C)[52,53]. In systems with strong ion pairing, the cation and anion exhibit similar diffusion rates, whereas discrepancies suggest weaker association or dynamic equilibria. As [**3**][X]$_2$ is dicationic, the measured D^- reflects the diffusion of the two independent anions. Free PF$_6^-$ and BF$_4^-$ have typical r_H values of 2.5-2.7 Å, while in the complexes, D^- values are 3.2 (PF$_6^-$) and 3.7 (BF$_4^-$), suggesting cation–anion interactions with a stronger interaction for BF$_4^-$.

Taken together, the ^{1}H and ^{19}F NMR chemical shifts, line broadening, and diffusion data consistently support stronger cation–anion interactions in the BF$_4^-$ complex compared to PF$_6^-$. The higher degree of association with BF$_4^-$ may arise from its greater ability to engage in hydrogen bonding, attributed to the higher electron localization on its fluorine atoms relative to PF$_6^-$ [54].

Anion activation and intermediate identification

To access tricationic Co^{III} species, we treated complexes [**3**][X]$_2$ (X = PF$_6^-$, BF$_4^-$) with AgX (X = PF$_6^-$, BF$_4^-$), known for its ability to abstract halides. The reactions were performed in CD_3CN to occupy the coordination vacancy created, and monitored by ^{1}H NMR spectroscopy (Fig. S23). This revealed the immediate and clean formation of the corresponding solvated complexes, [Co(κ^5-Py$_4$Im)(NCCD$_3$)][X]$_3$ ([**4**][X]$_3$; X = PF$_6^-$, BF$_4^-$).

https://doi.org/10.1038/s41467-026-69257-8

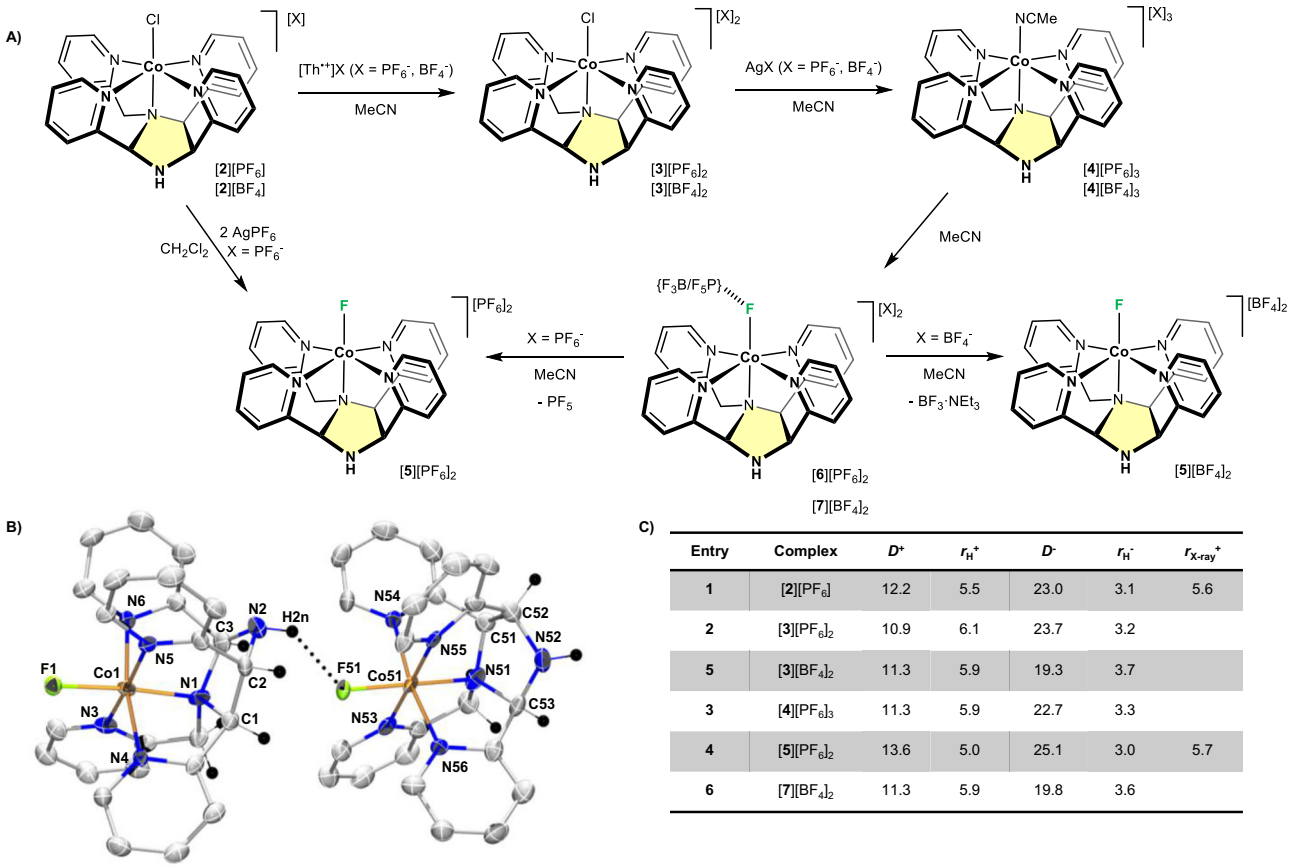

Entry	Complex	D^+	r_H^+	D^-	r_H^-	$r_{X\text{-}ray}^+$
1	[2][PF$_6$]	12.2	5.5	23.0	3.1	5.6
2	[3][PF$_6$]$_2$	10.9	6.1	23.7	3.2	
5	[3][BF$_4$]$_2$	11.3	5.9	19.3	3.7	
3	[4][PF$_6$]$_3$	11.3	5.9	22.7	3.3	
4	[5][PF$_6$]$_2$	13.6	5.0	25.1	3.0	5.7
6	[7][BF$_4$]$_2$	11.3	5.9	19.8	3.6	

Fig. 4 | Oxidation chemistry and ion-pairing effects in Co^{III} complexes. **A** Synthesis of complexes [Co(κ^5-Py$_4$Im)Cl][X]$_2$ ([**3**][X]$_2$, X = PF$_6$, BF$_4$), [Co(κ^5-Py$_4$Im)(NCMe)][X]$_3$ ([**4**][X]$_3$), [Co(κ^5-Py$_4$Im)F][X]$_2$ ([**5**][X]$_2$) [Co(κ^5-Py$_4$Im)(F − PF$_5$)][PF$_6$]$_2$ ([**6**][PF$_6$]$_2$), and [Co(κ^5-Py$_4$Im)(F − BF$_3$)][BF$_4$]$_2$ ([**7**][BF$_4$]$_2$). **B** Crystal structure of [Co(κ^5-Py$_4$Im)F][PF$_6$]$_2$ ([**5**][PF$_6$]$_2$) with displacement ellipsoids set to 50%. The two cations in the asymmetric unit are represented. Only hydrogen atoms on the imidazolidine ring are represented for clarity. **C** Table with diffusion coefficients (10^{10}, m^2·s^{-1}) and hydrodynamic radii (r_H, Å).

Complexes [**4**][X]$_3$ (X = PF$_6^-$, BF$_4^-$) were found to be unstable in solution, undergoing slow conversion to new diamagnetic species at room temperature. Notably, the reaction outcome strongly depends on the identity of the counteranion. For [**4**][PF$_6$]$_3$, the transformation proceeds slowly, with 50% conversion observed after 22 h at 25 °C in CD$_3$CN (Fig. S23), and requires a full week to reach completion. The resulting product was identified as an unexpected metal-fluoride complex, [Co^{III}(κ^5-Py$_4$Im)F][PF$_6$]$_2$ ([**5**][PF$_6$]$_2$, Fig. 4A). The PF$_6^-$ counterions were observed in the ^{31}P and ^{19}F NMR spectra. However, the ^{19}F NMR signal for the fluoride directly bonded to the cobalt (Co–F) was not observed, probably due to the large quadrupole coupling constant and nuclear spin (I = 7/2) of ^{59}Co, which can broaden the peaks into the baseline[55].

The solid-state structure of [**5**][PF$_6$]$_2$ revealed both enantiomers of the dication in the asymmetric unit (Fig. 4B), stabilized by an intermolecular hydrogen bond between the fluoride ligand of one molecule and the NH group of the other. However, DOSY and dilution studies (^{1}H NMR, 26.2 mM to 7 mM) indicate that this hydrogen bond is not retained in CD$_3$CN solution, where the complex exists as a monomer (Fig. S15).

Structurally, the cobalt center in [**5**][PF$_6$]$_2$ adopts an octahedral geometry, coordinated to four pyridine nitrogen atoms, the bridging imidazolidine nitrogen, and a terminal fluoride ligand. As expected for oxidation from Co^{II} to Co^{III}, the Co–N$_{py}$ bond lengths are shorter than those observed in [**2**]$_2$[CoCl$_4$][56,57]. The Co–F bond lengths (Co1-F1: 1.850(5); Co51-F51: 1.872(5) Å) fall within the reported range of Co^{III} terminal fluoride bonds (1.84–1.94)[55,58,59].

This transformation is particularly noteworthy because it involves activation of a P–F bond in the PF$_6^-$ counterion, an uncommon transformation for late transition metals. A plausible mechanism involves initial dissociation of the coordinated solvent in [**4**][PF$_6$]$_3$ to generate a vacant site, followed by inner-sphere coordination of PF$_6^-$[60]. Subsequent fluoride transfer to the metal and formal extrusion of PF$_5$ would directly yield the [**5**][PF$_6$]$_2$ as the final product. Although PF$_5$ was not directly observed by NMR spectroscopy, its formation is indirectly supported by the polymerization of THF when the reaction is performed in this solvent, consistent with the known Lewis acidity of PF$_5$.

Supporting this mechanism, [**5**][PF$_6$]$_2$ can also be synthesized directly by treating [**2**][PF$_6$] with two mol-equiv. of AgPF$_6$, in CH$_2$Cl$_2$, a non-coordinating solvent that does not compete for the vacant site. In this one-pot transformation, one equivalent of AgPF$_6$ abstracts the chloride ligand, while the second promotes oxidation of Co^{II} to Co^{III}.

To gain further insight into the proposed mechanism and identify a potential intermediate with PF$_6^-$ coordinated to the cobalt center, we varied the amount of AgPF$_6$ used in the reaction with [**4**][PF$_6$]$_3$. When only one mol-equiv. of AgPF$_6$ is used, trace amounts of an intermediate species are detected by NMR spectroscopy (Fig. S24). The concentration of this intermediate increases with the amount of AgPF$_6$ added and is proposed to be a Co^{III} complex with coordinated PF$_6^-$, [Co^{III}(κ^5-Py$_4$Im)(F-PF$_5$)][PF$_6$]$_2$ ([**6**][PF$_6$]$_2$), which then evolves to [**5**][PF$_6$]$_2$, supporting the stepwise formation of the Co-F bond via a PF$_6^-$-bound intermediate. At 4 mol-equiv. of AgPF$_6$, the reaction mixture consists of a 60:40 ratio of the acetonitrile adduct, [**4**][PF$_6$]$_3$, and [**6**][PF$_6$]$_2$, while at 8 mol-equiv., this ratio shifts to 17:83. Due to its transient

https://doi.org/10.1038/s41467-026-69257-8

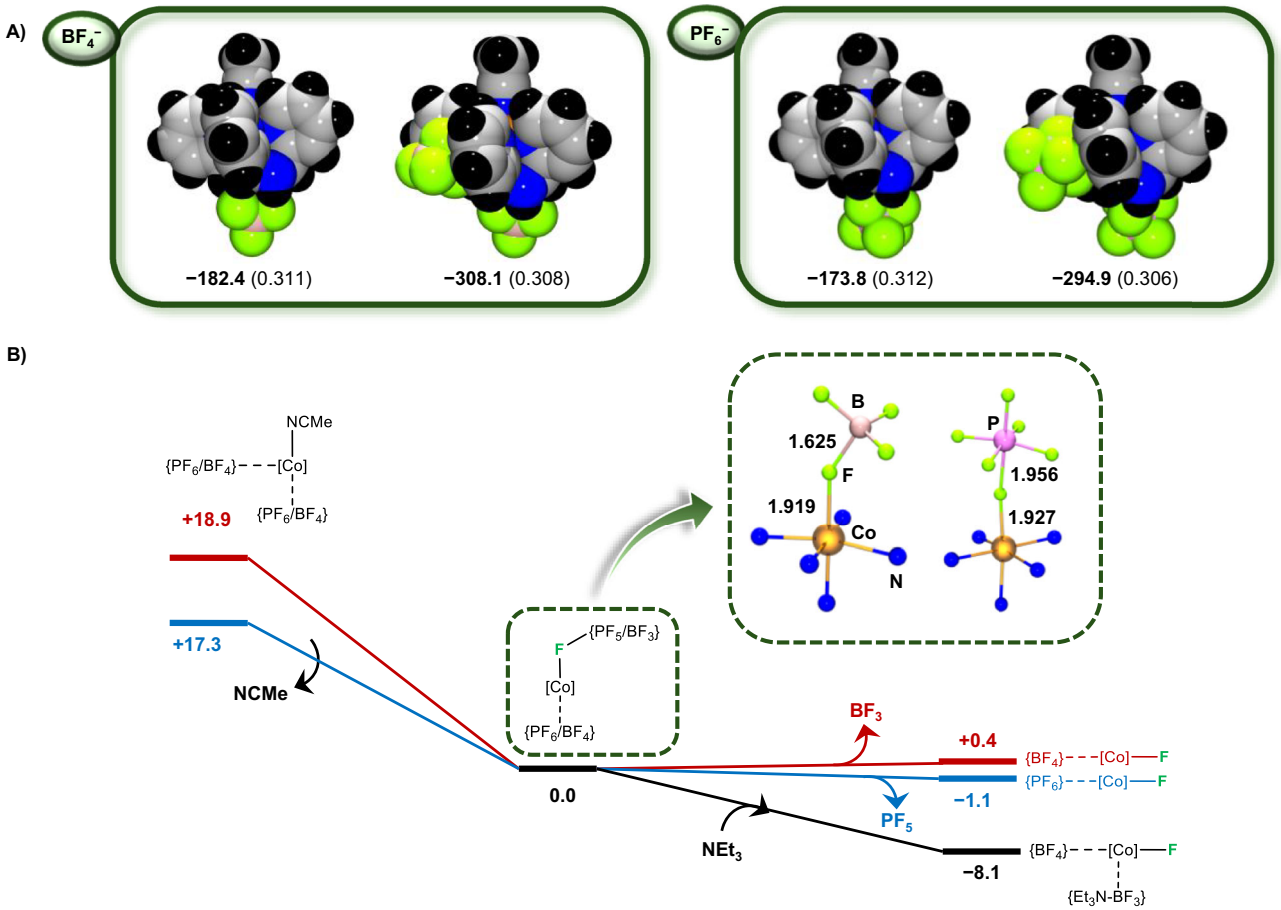

Fig. 5 | Computational analysis of ion pairing and anion activation (B3LYP-D3/Def2TZVP). A DFT-optimized structure and relative Gibbs free energies (Δ*G*, kcal·mol-1) for the ion-pairing of $[Co(\kappa^5\text{-}Py_4Im)(NCCH_3)]^{3+}$ ($[\mathbf{4}]^{3+}$) with PF_6^- or BF_4^-, modeled with one or two anions. Natural Bond Orbital (NBO) charges on the cobalt center are given in parentheses. **B** DFT-computed Gibbs free energy profile for the activation of PF_6^- (blue pathway) or BF_4^- (red pathway) starting from $[\mathbf{4}]^{3+}$ interacting with two anions. Relative Δ*G* values are given in kcal·mol^{-1}. The black pathway represents the assisted fluoride abstraction from $[\mathbf{7}]^{2+}$ in the presence of NEt_3. In the green inset: DFT-calculated structures of the anion-bound intermediates [**6**][PF_6]$_2$ and [**7**][BF_4]$_2$.

nature, [**6**][PF_6]$_2$ was characterized in situ by NMR spectroscopy at −40 °C.

In contrast, when BF_4^- is employed as the counterion, a different outcome is observed. The reaction leads to the formation of a stable anion-bound intermediate, $[Co^{III}(\kappa^5\text{-}Py_4Im)(F\text{-}BF_3)][BF_4]_2$ ([**7**][BF_4]$_2$), which does not undergo fluoride abstraction under the same conditions. Therefore, [**7**][BF_4]$_2$ can be cleanly isolated on a preparative scale in high yields. In the ^{19}F NMR spectrum, a very broad singlet is observed at −149.0 ppm ($LW_{1/2}$ = 153 Hz), significantly broader than that of free BF_4^- ($LW_{1/2}$ = 3 Hz) and high-field shifted, confirming strong interaction between the anion and the cobalt (Fig. S20).

Computational insights into anion activation mechanisms

The divergent reactivity observed for PF_6^- and BF_4^- was unexpected, particularly considering that BF_4^- is generally more susceptible to fluoride abstraction due to its lower fluoride ion affinity (FIA = 83.1 kcal·mol^{-1}) compared to PF_6^- (FIA = 94.9 kcal·mol^{-1})[60,61]. Yet, while PF_6^- undergoes clean fluoride transfer to form a stable Co−F complex, BF_4^- remains inert under identical conditions. To understand this counterintuitive behavior, we performed DFT calculations (B3LYP-D3/Def2TZVP) to evaluate the influence of ion pairing and supramolecular organization on anion activation.

We first modeled ion-pairing interactions between $[Co(\kappa^5\text{-}Py_4Im)(NCCH_3)]^{3+}$ ($[\mathbf{4}]^{3+}$) and either BF_4^- or PF_6^- using structures containing one or two associated anions (Fig. 5A). With one anion, BF_4^- displayed a slightly stronger interaction (−182.4 kcal·mol^{-1}) than PF_6^- (−173.8 kcal·mol^{-1}), consistent with more persistent ion pairing. In both cases, the first anion is positioned directly beneath the imidazolidine ring, stabilized by hydrogen bonding interactions between its fluorine atoms and the ligand's protic cavity. This consistent localization of the anion beneath the imidazolidine ring underscores the role of the Py_4Im ligand in shaping a directional binding pocket. The protic cavity, defined by the NH and CH_2 groups of the imidazolidine ring, acts as a hydrogen-bonding anchor that stabilizes the anion in a specific orientation.

Addition of a second anion preserved this trend, though the absolute binding energies were attenuated due to increased electrostatic repulsion. The second anion preferentially resides in the cleft between two flanking pyridine rings, further supporting a defined spatial organization driven by electrostatic and hydrogen bonding interactions. In all cases, natural bond orbital (NBO) analysis revealed similar cobalt partial charges (q ≈ +0.31), indicating that the electronic structure of the metal center remains largely unaffected by the identity or number of associated anions. These results suggest that the observed differences in reactivity are primarily governed by anion coordination dynamics rather than changes in the intrinsic electronic properties of the cobalt complex.

We next investigated the thermodynamics of fluoride abstraction from PF_6^- and BF_4^- using the single-anion model, which allowed direct comparison since both reactions converge on the same Co−F product

https://doi.org/10.1038/s41467-026-69257-8

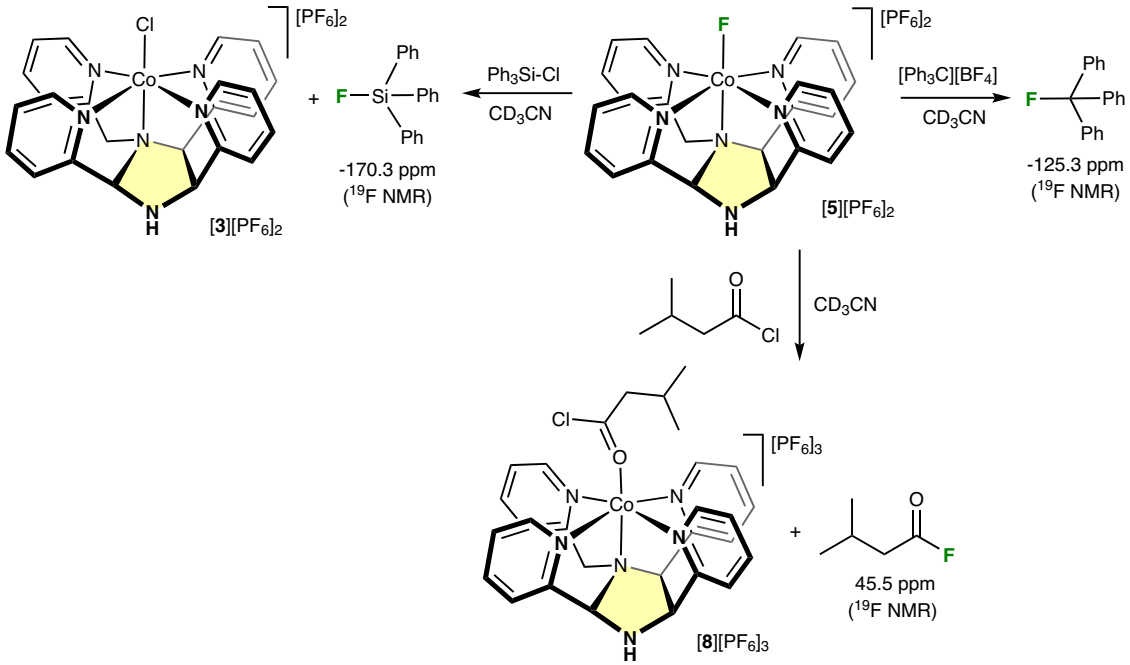

Fig. 6 | Fluoride transfer reactivity of the Co^{III}F complex. Fluoride transfer from [**5**][PF_6]$_2$ to trityl tetrafluoroborate, triphenylchlorosilane, and isovaleryl chloride, forming the corresponding fluoride products and the Co^{III} complexes [**3**][PF_6]$_2$ or [**8**][PF_6]$_3$.

(Fig. S38). Fluoride abstraction from PF_6^- was exergonic by −3.8 kcal·mol^{-1}, while the corresponding reaction with BF_4^- was also favorable, though less so (−1.5 kcal·mol^{-1}).

While the interaction with one anion offered a useful starting point for understanding intrinsic bond cleavage thermodynamics, it could not fully explain the lack of reactivity observed experimentally for BF_4^-. To gain a more realistic picture of the system, and better understand the role of ion-pairing, we next introduced a second anion into the computational model (Fig. 5B). With two anions, fluoride abstraction from PF_6^- remained exergonic (−1.1 kcal·mol^{-1}, blue pathway), consistent with its observed reactivity, whereas the analogous transformation involving BF_4^- became slightly endergonic (+0.4 kcal·mol^{-1}, red pathway). This change highlights how tight ion-pairing in the BF_4^- system stabilizes the starting complex and disfavors bond cleavage, even when the intrinsic B–F bond is weaker than P–F. The computational results thus provide a molecular-level explanation for the experimentally observed lack of reactivity of BF_4^- and validate the hypothesis that anion–cation interactions critically modulate WCA activation.

Further support comes from the calculated structures of the PF_6^-- and BF_4^--bound intermediates, [**6**][PF_6]$_2$ and [**7**][BF_4]$_2$, in the two-anion model (Fig. 5B). Both feature Co–F distances (approx. 1.92 Å) consistent with terminal Co–F bonds, and significantly elongated P–F (1.956 Å) and B–F (1.625 Å) bonds relative to the free anions, indicating substantial bond weakening. These features are consistent with their assignment as late-stage intermediates in fluoride transfer.

To test whether the BF_4^- barrier could be overcome experimentally, we examined the use of an external Lewis base to trap the BF_3 byproduct. DFT calculations showed that coordination of triethylamine (NEt_3) to [**7**][BF_4]$_2$, forming a BF_3·NEt_3 adduct, renders the fluoride abstraction process exergonic ($\Delta G = -8.1$ kcal·mol^{-1}; Fig. 5B, black pathway). Encouraged by this result, we performed the reaction experimentally in the presence of excess NEt_3, which led to the formation of the Co–F complex [**5**][BF_4]$_2$, as confirmed by NMR spectroscopy. These results demonstrate that while BF_4^- is inert toward fluoride abstraction under standard conditions, its activation can be induced through Lewis base-assisted fluoride abstraction, providing a viable strategy to promote WCA activation in late transition metal systems.

Fluoride transfer reactivity of the Co–F

To evaluate the fluoride-donor ability of [**5**][PF_6]$_2$, we first treated the complex with trityl tetrafluoroborate ([Ph_3C][BF_4]), which cleanly generated trityl fluoride (Fig. 6), observed at −125.3 ppm in the ^{19}F NMR spectrum (Fig. S26). When excess [Ph_3C][BF_4] was used, the PF_6^- resonance disappeared entirely, indicating consumption of both the Co–F ligand and the PF_6^- anions present in solution. We next examined triphenylchlorosilane (Ph_3SiCl) as a heteroatom-based electrophile. Reaction of [**5**][PF_6]$_2$ with Ph_3SiCl cleanly generated triphenylfluorosilane (Ph_3SiF; Fig. 6), detected at −170.3 ppm in the ^{19}F NMR spectrum (Fig. S28). The NMR tube showed complete conversion of [**5**][PF_6]$_2$ into [**3**][PF_6]$_2$ (Fig. S27), consistent with chloride transfer from the silane to the cobalt center accompanying fluoride delivery to silicon.

Treatment of [**5**][PF_6]$_2$ with isovaleryl chloride also resulted in fluoride transfer, forming isovaleryl fluoride (45.5 ppm in the ^{19}F NMR spectrum, Fig. S30). In parallel, [**5**][PF_6]$_2$ was fully converted into a new Co^{III} complex, [**8**][PF_6]$_3$ (Fig. 6), identified by NMR spectroscopy and HR-ESI mass spectrometry as the acyl-chloride-coordinated complex (Figs. S29, S31). This outcome is consistent with chloride rebound to cobalt after fluoride delivery to the acyl chloride. Together, these results demonstrate that the Co–F bond formed upon PF_6^- activation functions as a nucleophilic fluoride source toward carbocationic, silyl, and acyl electrophiles, revealing reactivity enabled by selective PF_6^- activation at a cobalt center.

This work reveals that cation-anion interactions profoundly influence the reactivity of WCAs, challenging the assumption that their behavior is dictated solely by intrinsic thermodynamic stability. Using a macrocyclic Py_4Im cobalt platform, we show that PF_6^- and BF_4^-, two archetypal WCAs, exhibit contrasting reactivity toward a highly charged Co^{III} center. While PF_6^- undergoes clean fluoride abstraction under mild conditions to form a terminal Co–F complex, BF_4^- remains inert unless a Lewis base is introduced to trap the BF_3 byproduct. These results provide a rare example of selective WCA activation at a

late transition metal site and establish a blueprint for tuning reactivity through counterion choice.

Crucially, this divergence is not dictated by fluoride ion affinity, BF_4^- is in fact more labile, but by the strength and geometry of cation–anion pairing. As shown by DFT and DOSY data, BF_4^- forms tighter ion pairs with the Co^{III} center, stabilizing the system and inhibiting B–F bond cleavage. In contrast, the weaker ion pairing of PF_6^- facilitates anion activation. Importantly, these interactions are not isotropic: the spatial confinement and hydrogen-bonding capability of the Py_4Im ligand, particularly its protic imidazolidine cavity, create a directional microenvironment that guides anion positioning and modulates reactivity.

This demonstrates that macrocyclic topology and ligand-centered hydrogen bonding can be leveraged to define anion trajectory and engagement. The strategic placement of proton donors around the reactive site offers a generalizable approach to preorganize weakly coordinating anions in catalytically relevant orientations, a principle that may be extended to design ligand frameworks for controlled ion-pairing and selective bond activation. This highlights the value of ligand design not only in stabilizing high-valent species but also in directing supramolecular interactions that influence bond activation pathways.

Method

General experimental procedures

All manipulations were performed under an argon atmosphere using standard Schlenk techniques and glovebox facilities. C_6D_6 and CD_3CN were dried over 4 Å molecular sieves and degassed through three freeze-pump-thaw cycles. Hexane, Et_2O and toluene were collected from an M. Braun MB-SPS-800 solvent purification system. MeOH was dried over magnesium, distilled, and degassed before use. Anhydrous CH_3CN was purchased from either Merck or Acros. All other reagents and solvents were acquired commercially and used as received unless otherwise stated. $CoCl_2$ was dried under vacuum prior to use. Deuterated solvents were dried over molecular sieves and degassed by freeze–pump–thaw cycles. Detailed synthetic procedures and full characterization data are provided in the Supplementary Information.

Spectroscopic and analytical methods

Elemental analyses were performed using a Perkin–Elmer 2400 CHNS/O analyzer. Mass spectra and high-resolution mass spectra of complexes were acquired on a Bruker Esquire3000 plus (ESI+) and a Bruker MicroTOF-Q (ESI+) spectrometers, respectively. Molar conductivities were measured using a Philips PW 9501/01 conductometer.

NMR spectra were recorded on Bruker AV300, AV400 and AV500 spectrometers operating at 300.13, 400.13 MHz and 500.13 MHz, respectively, for ^{1}H. Chemical shifts are quoted in ppm relative to $SiMe_4$, using the internal signal of the deuterated solvent (for ^{1}H and ^{13}C), to 85% H_3PO_4 (external, for ^{31}P), to $CFCl_3$ (external, for ^{19}F), and to $BF_3{\cdot}OEt_2$ (external, for ^{11}B).

Paramagnetic ^{1}H NMR spectra were analyzed using T_1 relaxation time measurements, linewidths at half-height, and COSY experiments. The T_1 value for each signal was measured with a sweep width of 100 ppm centered on the group of signals within the sweep width. Initially, the T_1 value for each signal was estimated using the t1ir1d pulse program in order to set an appropriate D1 value (five times the estimated T_1 value) and a variable delay list for measuring an accurate T_1 value using the t1ir pulse program. Proton environments were classified based on correlation with metal–proton distances derived from crystallographic data.

DOSY NMR measurements

Diffusion-ordered NMR spectroscopy (DOSY) experiments were performed using Pulsed-Field Gradient Spin-Echo (PFGSE) sequences and analyzed with Bruker TopSpin software. All spectra were acquired spinning at 27 °C. The variation of the intensity of a selected signal in the ^{1}H or ^{19}F NMR spectra (I) as a function of the gradient strength (G) is described by the equation: $Ln(I/I^0) = -\gamma^2\delta^2Gi^2(\Delta-\delta/3)D$, where γ = gyromagnetic ratio of the proton, δ = length of the gradient pulse, Gi = gradient strength, Δ = delay between the midpoints of the gradients, and D = diffusion coefficient[62]. Before recording the DOSY experiment, the values of δ (small delta) and Δ (big delta) were optimized for each complex by using the 1D pulse sequence for diffusion measurements (ledbpgp2s1d, δ (2 × P30) and Δ (d20), Bruker's software). The selected values provided a considerable reduction of the intensity of the signal, while remaining sufficient signal for integration. Next, the 2D DOSY experiment (ledbpgp2s pulse sequence) was recorded using the optimized δ and Δ values, with the G incremented over 16 steps. Data were analyzed with Bruker's software, which directly provided the diffusion coefficient (D). The quality of the data was tested by representation $Ln(I/I^0)$ versus G^2, which gave an excellent fit to a straight line in all the cases. Hydrodynamic radii (r_H) were calculated from the modified Stokes–Einstein equation: $D = \frac{\kappa T}{(f_s c)\pi\eta r_H}$, where the appropriate c factor: $c = \frac{6}{1+0.695b^{2.234}}$ ($b = \frac{r_{solv}}{r_H}$) was calculated by iterative calculation[52,53]. For the paramagnetic complex, [**2**][PF_6], diffusion data were acquired using the signals at 21.8 and 22.5 ppm, which showed suitable line widths and relaxation times according to established criteria[63].

Magnetic and electrochemical measurements

Magnetic moments were calculated using Evans' method[64]. Cyclic voltammetry measurements were collected using a WaveNow Wireless potentiostat (Pine Research Instrumentation) in an undivided three-electrode cell, with a glassy carbon working electrode (3 mm diameter), a platinum wire counter electrode, and a silver wire pseudoreference electrode. Glassy carbon electrodes were polished using a Milli-Q water slurry of 0.05 µm alumina powder, rinsed and sonicated in Milli-Q water, and finally rinsed with acetone. A 0.1 M solution of tetrabutylammonium hexafluorophosphate ([NBu_4][PF_6]) or tetrabutylammonium tetrafluoroborate ([NBu_4][BF_4]) in acetonitrile was used as the supporting electrolyte for measurements involving [**2**][PF_6] and [**2**][BF_4], respectively. Ferrocene was added as an internal reference after initial data collection.

X-ray crystallography

Intensity measurements were collected with a Siemens Smart Apex ([**2**]$_2$[$CoCl_4$]·NCMe) or a Bruker D8 Venture ([**5**][PF_6]$_2$·1.5NCMe) diffractometers, with $Mo_{K\alpha}$ radiation at 100 K. Data were collected using ω-scans (and φ-scans for ([**5**][PF_6]$_2$·1.5NCMe)) and narrow frame strategies. A semi-empirical absorption correction was applied to the data sets with the multi-scan[65] methods. The structures were solved by direct methods with SHELXT-2014[66] and refined by full-matrix least-squares on F^2 with the program SHELXL-2016[67], in the WINGX[68] package. Full crystallographic data are provided in the Supplementary Information.

Computational details

DFT geometry optimizations and thermochemical calculations were carried out with the Gaussian 09 program package[69], using the B3LYP-D3 hybrid functional[70–73]. All calculations were performed in the gas phase with the Def2TZVP triple zeta basis set[74,75].

Data availability

Crystallographic data for the structures reported in this Article have been deposited at the Cambridge Crystallographic Data Center, under deposition numbers CCDC 2472803 ([**2**]$_2$[$CoCl_4$]) and 2472804 ([**5**][PF_6]$_2$). Copies of the data can be obtained free of charge via https://www.ccdc.cam.ac.uk/structures/. Source Data are provided with this manuscript, including optimized Cartesian coordinates from DFT calculations in an Excel file. All other data supporting the findings of this

study are included in this Article and its Supplementary Information. All data are available from the corresponding author upon request. Source data are provided with this paper.

References

1. Chianese, A. R., Lee, S. J. & Gagné, M. R. Electrophilic activation of alkenes by platinum(II): so much more than a slow version of palladium(II). *Angew. Chem. Int. Ed.* **46**, 4042–4059 (2007).
2. Patel, M., Ajay, U., Padala, K. & Naveen, T. Recent advances in cobalt-catalyzed functionalization of unactivated olefins. *Asian J. Org. Chem.* **11**, e202200201 (2022).
3. Yadav, J. S., Antony, A., Rao, T. S. & Subba Reddy, B. V. Recent progress in transition metal catalysed hydrofunctionalisation of less activated olefins. *J. Organomet. Chem.* **696**, 16–36 (2011).
4. Hahn, C. Enhancing electrophilic alkene activation by increasing the positive net charge in transition-metal complexes and application in homogeneous catalysis. *Chem. – Eur. J.* **10**, 5888–5899 (2004).
5. Keith, J. A. & Henry, P. M. The mechanism of the wacker reaction: a tale of two hydroxypalladations. *Angew. Chem. Int. Ed.* **48**, 9038–9049 (2009).
6. Song, G., Wang, F. & Li, X. C.–C. C–O and C–N bond formation via rhodium(iii)-catalyzed oxidative C–H activation. *Chem. Soc. Rev.* **41**, 3651–3678 (2012).
7. Lukasevics, L., Cizikovs, A. & Grigorjeva, L. C–H bond functionalization by high-valent cobalt catalysis: current progress, challenges and future perspectives. *Chem. Commun.* **57**, 10827–10841 (2021).
8. Anjali, S., Devi, P. S. & Anilkumar, G. Recent advances in cobalt-catalyzed oxidative C–H activation. *Chem. Rec.* **25**, e202500009 (2025).
9. Planas, O. et al. Isolation of key organometallic aryl-Co(III) intermediates in cobalt-catalyzed C(sp2)–H functionalizations and new insights into alkyne annulation reaction mechanisms. *J. Am. Chem. Soc.* **138**, 14388–14397 (2016).
10. van Leest, N. P., van der Vlugt, J. I. & de Bruin, B. Catalytic chemoselective sulfimidation with an electrophilic [CoIII(TAML)]-nitrene radical complex**. *Chem. – Eur. J.* **27**, 371–378 (2021).
11. Meeus, E. J. et al. Styrene aziridination with [CoIII(TAMLred)]– in water: understanding and preventing epoxidation via nitrene hydrolysis. *Chem. Catal.* **3**, 100700 (2023).
12. Grigorjeva, L. & Daugulis, O. Cobalt-catalyzed, aminoquinoline-directed C(sp2)H bond alkenylation by alkynes. *Angew. Chem. Int. Ed.* **53**, 10209–10212 (2014).
13. Das, A. et al. High-valent cobalt-difluoride in oxidative fluorination of saturated hydrocarbons. *Angew. Chem. Int. Ed.* **64**, e202421157 (2025).
14. Díaz-Torres, R. & Alvarez, S. Coordinating ability of anions and solvents towards transition metals and lanthanides. *Dalton Trans* **40**, 10742–10750 (2011).
15. Riddlestone, I. M., Kraft, A., Schaefer, J. & Krossing, I. Taming the cationic beast: novel developments in the synthesis and application of weakly coordinating anions. *Angew. Chem. Int. Ed.* **57**, 13982–14024 (2018).
16. Geiger, W. E. & Barrière, F. Organometallic electrochemistry based on electrolytes containing weakly-coordinating fluoroarylborate anions. *Acc. Chem. Res.* **43**, 1030–1039 (2010).
17. Clarke, C. J., Clayton, T., Palmer, M. J., Lovelock, K. R. J. & Licence, P. A thermophysical investigation of weakly coordinated metals in ionic liquids. *Chem. Sci.* **15**, 13832–13840 (2024).
18. Agahi, R., Challinor, A. J., Carter, N. B. & Thomas, S. P. Earth-abundant metal catalysis enabled by counterion activation. *Org. Lett.* **21**, 993–997 (2019).
19. Lucarini, F. et al. Rationalizing photo-triggered hydrogen evolution using polypyridine cobalt complexes: substituent effects on hexadentate chelating ligands. *ChemSusChem.* **14**, 1874–1885 (2021).
20. Stefankiewicz, A. R. et al. Quaterpyridine ligands forming helical complexes of mono- and dinuclear (Helicate) forms. *Eur. J. Inorg. Chem.* **2008**, 2910–2920 (2008).
21. Bonyhady, S. J. et al. Iron and cobalt diazoalkane complexes supported by β-diketiminate ligands: a synthetic, spectroscopic, and computational investigation. *Inorg. Chem.* **57**, 5959–5972 (2018).
22. Farooq, O. & Tiers, G. V. D. Alkali metal salts of perfluorinated complex anions. Effective reagents for nucleophilic fluorination. *J. Org. Chem.* **59**, 2122–2124 (1994).
23. Jin, Z., Xu, B., DiMagno, S. G. & Hammond, G. B. Replacement of BF4– by PF6– makes Selectfluor greener. *J. Fluor. Chem.* **143**, 226–230 (2012).
24. Krossing, I. & Raabe, I. Relative stabilities of weakly coordinating anions: a computational study. *Chem. – Eur. J.* **10**, 5017–5030 (2004).
25. Larsson, J. M. & Szabó, K. J. Mechanistic investigation of the palladium-catalyzed synthesis of allylic silanes and boronates from allylic alcohols. *J. Am. Chem. Soc.* **135**, 443–455 (2013).
26. Yoshida, T., Ohta, M., Emmei, T., Kodama, T. & Tobisu, M. Cationic rhodium(I) tetrafluoroborate catalyzed intramolecular carbofluorination of alkenes via acyl fluoride C–F bond activation. *Angew. Chem. Int. Ed.* **62**, e202303657 (2023).
27. Thompson, S. J., Bailey, P. M., White, C. & Maitlis, P. M. Solvolysis of the hexafluorophosphate ion and the structure of [Tris(μ-difluorophosphato)bis(penta-methylcyclopentadienylrhodium)] Hexafluorophosphate. *Angew. Chem. Int. Ed. Engl.* **15**, 490–491 (1976).
28. Rowsey, R. A., Hilgar, J. D. & Romero, N. A. Silylimidazolium hexafluorophosphate salts as synthetic precursors to N-heterocyclic carbene pentafluorophosphorus adducts. *Org. Lett.* **26**, 4750–4755 (2024).
29. Jordan, R. F., Dasher, W. E. & Echols, S. F. Reactive cationic dicyclopentadienyl zirconium(IV) complexes. *J. Am. Chem. Soc.* **108**, 1718–1719 (1986).
30. Thomas, B. J., Mitchell, J. F., Theopold, K. H. & Leafy, J. A. Synthesis and structure determination of [Cp*4Cr4(μ-F)5Cl2]PF6. A tetranuclear chromium complex formed by fluoride abstraction from hexafluorophosphate. *J. Organomet. Chem.* **348**, 333–342 (1988).
31. Kuppuswamy, S. et al. One-electron oxidation chemistry and subsequent reactivity of diiron imido complexes. *Inorg. Chem.* **53**, 5429–5437 (2014).
32. Zhang, H., Hatzis, G. P., Dickie, D. A., Moore, C. E. & Thomas, C. M. Redox chemistry and H-atom abstraction reactivity of a terminal zirconium(iv) oxo compound mediated by an appended cobalt(i) center. *Chem. Sci.* **11**, 10729–10736 (2020).
33. Cresswell, A. J., Davies, S. G., Roberts, P. M. & Thomson, J. E. Beyond the balz–schiemann reaction: the utility of tetrafluoroborates and boron trifluoride as nucleophilic fluoride sources. *Chem. Rev.* **115**, 566–611 (2015).
34. Kiaku, C. et al. eFluorination of activated alcohols using collidinium tetrafluoroborate. *Org. Lett.* **26**, 2697–2701 (2024).
35. Garg, A., Haswell, A. & Hopkinson, M. N. C.–F. Bond insertion: an emerging strategy for constructing fluorinated molecules. *Chem. – Eur. J.* **30**, e202304229 (2024).
36. Wei, L., Li, Q.-H. & Wang, C.-J. Copper(I)-catalyzed asymmetric 1,3-dipolar cycloaddition of azomethine ylides with fluorinated imines: the expanded scope and mechanism insights. *J. Org. Chem.* **83**, 11814–11824 (2018).
37. Yu, B. et al. Enantioselective synthesis of chiral imidazolidine derivatives by asymmetric silver/xing-phos-catalyzed homo-1,3-dipolar [3+2] cycloaddition of azomethine ylides. *Adv. Synth. Catal.* **359**, 3577–3584 (2017).
38. Thorarinsdottir, A. E. & Nocera, D. G. Energy catalysis needs ligands with high oxidative stability. *Chem. Catal.* **1**, 32–43 (2021).
39. Champouret, Y. D. M. et al. Factors affecting imine coordination in (iminoterpyridine)MX2 (M = Fe, Co, Ni, Zn): synthesis, structures,

DFT calculations and ethylene oligomerisation studies. *New J. Chem.* **31**, 75–85 (2007).
40. Boniolo, M. et al. Electronic and geometric structure effects on one-electron oxidation of first-row transition metals in the same ligand framework. *Dalton Trans* **50**, 660–674 (2021).
41. Wasylenko, D. J., Ganesamoorthy, C., Borau-Garcia, J. & Berlinguette, C. P. Electrochemical evidence for catalytic water oxidation mediated by a high-valent cobalt complex. *Chem. Commun.* **47**, 4249–4251 (2011).
42. Ou, Y.-J. et al. A series of temperature-dependent CdII-complexes containing an important family of N-rich heterocycles from in situ conversion of pyridine-type Schiff base. *RSC Adv.* **5**, 27743–27751 (2015).
43. Paul, A. et al. Tetranuclear and 1D polymeric Cd(II) complexes with a tetrapyridyl imidazolidine ligand: synthesis, structure, and fluorescence sensing activity. *Cryst. Growth Des.* **20**, 2904–2913 (2020).
44. Ou, Y.-J. et al. CdII-mediated efficient synthesis and complexation of asymmetric tetra-(2-pyridine)-substituted imidazolidine. *Cryst. Growth Des.* **14**, 5339–5343 (2014).
45. Tarifa, L. et al. Iridium-catalyzed regio- and diastereoselective synthesis of c-substituted piperazines. *ACS Catal.* **13**, 3148–3152 (2023).
46. Solomon, I. Relaxation processes in a system of two spins. *Phys. Rev.* **99**, 559–565 (1955).
47. Lehr, M. et al. A paramagnetic NMR spectroscopy toolbox for the characterisation of paramagnetic/spin-crossover coordination complexes and metal–organic cages. *Angew. Chem. Int. Ed.* **59**, 19344–19351 (2020).
48. Amouri, H. et al. Host–guest interactions: design strategy and structure of an unusual cobalt cage that encapsulates a tetrafluoroborate anion. *Angew. Chem. Int. Ed.* **44**, 4543–4546 (2005).
49. McConnell, A. J., Aitchison, C. M., Grommet, A. B. & Nitschke, J. R. Subcomponent exchange transforms an FeII4L4 cage from high- to low-spin, switching guest release in a two-cage system. *J. Am. Chem. Soc.* **139**, 6294–6297 (2017).
50. Tidmarsh, I. S. et al. Further investigations into tetrahedral M4L6 cage complexes containing guest anions: new structures and NMR spectroscopic studies. *New J. Chem.* **33**, 366–375 (2009).
51. Boduszek, B. & Shine, H. J. Preparation of solid thianthrene cation radical tetrafluoroborate. *J. Org. Chem.* **53**, 5142–5143 (1988).
52. Martínez-Alonso, M. et al. Analysis of ion pairing in solid state and solution in p-cymene ruthenium complexes. *Inorg. Chem.* **59,**, 14171–14183 (2020).
53. Zuccaccia, D. & Macchioni, A. An accurate methodology to identify the level of aggregation in solution by PGSE NMR measurements: the case of half-sandwich diamino ruthenium(II) salts. *Organometallics* **24**, 3476–3486 (2005).
54. Giron, R. G. P. & Ferguson, G. S. Tetrafluoroborate and hexafluorophosphate ions are not interchangeable: a density functional theory comparison of hydrogen bonding. *ChemistrySelect* **2**, 10895–10901 (2017).
55. Leclerc, M. C. et al. Perfluoroalkyl cobalt(III) fluoride and bis(perfluoroalkyl) complexes: catalytic fluorination and selective difluorocarbene formation. *J. Am. Chem. Soc.* **137**, 16064–16073 (2015).
56. Raithel, A. L., Kim, T.-Y., Nielsen, K. C., Staples, R. J. & Hamann, T. W. Low-spin cobalt(ii) redox shuttle by isocyanide coordination. *Sustain. Energy Fuels* **4**, 2497–2507 (2020).
57. Kashif, M. K. et al. A new direction in dye-sensitized solar cells redox mediator development: in situ fine-tuning of the cobalt(II)/(III) redox potential through lewis base interactions. *J. Am. Chem. Soc.* **134**, 16646–16653 (2012).
58. Blower, P. J. et al. Exploring transition metal fluoride chelates – synthesis, properties and prospects towards potential PET probes. *Dalton Trans* **48**, 6767–6776 (2019).
59. Lian, Z. et al. Imine-assisted C–F bond activation using low-valent cobalt compounds supported by trimethylphosphine ligands and formation of novel organic fluorides. *Dalton Trans* **39**, 9523–9529 (2010).
60. Reedijk, J. Formation of fluoride-containing coordination compounds by decomposition of transition-metal tetrafluoroborates. *Comments Inorg. Chem.* **1**, 379–389 (1982).
61. Christe, K. O. et al. On a quantitative scale for Lewis acidity and recent progress in polynitrogen chemistry. *J. Fluor. Chem.* **101**, 151–153 (2000).
62. Pregosin, P. S., Kumar, P. G. A. & Fernández, I. Pulsed gradient spin –echo (PGSE) diffusion and^{1} H,^{19} F Heteronuclear Overhauser Spectroscopy (HOESY) NMR methods in inorganic and organometallic chemistry: something old and something new. *Chem. Rev.* **105**, 2977–2998 (2005).
63. Crockett, M. P., Zhang, H., Thomas, C. M. & Byers, J. A. Adding diffusion ordered NMR spectroscopy (DOSY) to the arsenal for characterizing paramagnetic complexes. *Chem. Commun.* **55**, 14426–14429 (2019).
64. Evans, D. F. 400. The determination of the paramagnetic susceptibility of substances in solution by nuclear magnetic resonance. *J. Chem. Soc. Resumed* https://doi.org/10.1039/JR9590002003 (1959).
65. Sheldrick, G.M. SADABS, Program for Bruker area detector absorption correction. Bruker AXS, (Madison, WI USA, 1997).
66. Sheldrick, G. M. *SHELXT*– Integrated space-group and crystal-structure determination. *Acta Crystallogr. Sect. Found. Adv.* **71**, 3–8 (2015).
67. Sheldrick, G. M. Crystal structure refinement with *SHELXL*. *Acta Crystallogr. Sect. C Struct. Chem.* **71**, 3–8 (2015).
68. Farrugia, L. J. *WinGX* and *ORTEP for Windows*: an update. *J. Appl. Crystallogr.* **45**, 849–854 (2012).
69. Gaussian 09 et al Gaussian, Inc., (Wallingford, CT, 2011).
70. Lee, C., Yang, W. & Parr, R. G. Development of the Colle-Salvetti correlation-energy formula into a functional of the electron density. *Phys. Rev. B* **37**, 785–789 (1988).
71. Becke, A. D. A new mixing of Hartree–Fock and local density-functional theories. *J. Chem. Phys.* **98**, 1372–1377 (1993).
72. Becke, A. D. Density-functional thermochemistry. III. The role of exact exchange. *J. Chem. Phys.* **98**, 5648–5652 (1993).
73. Grimme, S., Antony, J., Ehrlich, S. & Krieg, H. A consistent and accurate ab initio parametrization of density functional dispersion correction (DFT-D) for the 94 elements H-Pu. *J. Chem. Phys.* **132**, 154104 (2010).
74. Weigend, F. & Ahlrichs, R. Balanced basis sets of split valence, triple zeta valence and quadruple zeta valence quality for H to Rn: Design and assessment of accuracy. *Phys. Chem. Chem. Phys.* **7**, 3297 (2005).
75. Weigend, F. Accurate Coulomb-fitting basis sets for H to Rn. *Phys. Chem. Chem. Phys.* **8**, 1057 (2006).

Acknowledgments

This work was primarily supported by MCIN/AEI/10.13039/501100011033 (PID2020-119512GB-I00; PID2023-148472NB-I00 and OASIS, RED2022-134074; C.T., A.M.G.) and Gobierno de Aragon/FEDER, EU (E50_23R; C.T., A.M.G.). A.M.G. is thankful for Grant RYC2021-033807-I, funded by MCIN/AEI/10.13039/501100011033 and NextGenerationEU, and 2024ICT331, funded by CSIC (Ayudas Incorporación Científicos Titulares OPIs). L.T. thanks MICIIN/FEDER for an FPI fellowship. The "Centro de Supercomputación de Galicia (CESGA)" is also gratefully acknowledged for the generous allocation of time.

Author contributions

A.M.G. and C.T. conceptualized the work, provided resources and supervision. L.T. and J.C., who contributed equally to this work,

performed the investigations (synthesis and characterization) and analyzed the experimental data. All crystallographic studies and DFT calculations were performed by J.A.L. The original draft was written by A.M.G., and reviewing and editing were done with contributions by all authors.

Competing interests
The authors declare no competing interests.

Additional information
Supplementary information The online version contains supplementary material available at https://doi.org/10.1038/s41467-026-69257-8.

Correspondence and requests for materials should be addressed to Cristina Tejel or Ana M. Geer.

Peer review information *Nature Communications* thanks Hui Gao, Basker Sundararaju, and the other anonymous reviewer(s) for their contribution to the peer review of this work. A peer review file is available.